JOURNAL OF GEOPHYSICAL RESEARCH, VOL. 89, NO. A5, PAGES 2891–2906, MAY 1, 1984

Electron Precipitation Zones Around Major Ground-Based VLF Signal Sources

U. S. INAN, H. C. CHANG, AND R. A. HELLIWELL

Space, Telecommunications and Radioscience Laboratory, Stanford University

The spatial distribution of electron precipitation induced by VLF signals from ground-based transmitters is determined by using a test particle computer model of the gyroresonant wave-particle interaction (Inan et al., 1982). The results are presented as contours of energy flux on a map of the region around each transmitter. It is shown that the size of the precipitation zones is a strong function of the geographic location of the transmitter, as well as its radiated power and operating frequency. In general, the precipitation zones are much wider in longitude than in latitude and are oriented along lines of constant geomagnetic latitude. Assuming backscatter and/or wave echoing, precipitation zones around the points that are magnetically conjugate to the sources are also estimated. The results presented can be used to interpret satellite- or ground-based measurements of the precipitation induced by ground-based VLF transmitters.

1. INTRODUCTION

Resonant interactions with whistler mode waves have long been identified as an important loss mechanism for the radiation belt particles at mid to low latitudes. These waves can be roughly divided into two classes: (1) waves that are of magnetospheric origin, such as plasmaspheric hiss and VLF chorus, and (2) waves that originate on the ground or in the atmosphere such as lightning-induced whistlers, VLF transmitter signals, and emissions triggered by these signals. In this paper, we shall be concerned with electron precipitation induced by signals from ground-based VLF transmitters.

In recent years, increased attention has been given to the problem of energetic particle precipitation induced by manmade VLF waves. Satellite observations of narrow peaks in the energy spectra of precipitating electrons observed in the drift loss cone have by inference been associated with monochromatic VLF signal sources [*Imhof et al.*, 1974, 1981*a*, *b*; *Vampola and Kuck*, 1978]. More recently, during experiments involving controlled injection of VLF signals from a ground-based VLF transmitter, precipitating electrons were directly observed in the bounce loss cone [*Imhof et al.*, 1983]. While these observations indicate that manmade signal sources do contibute to the precipitation of electrons out of the belts, the relative contribution of such waves as compared with natural wave activity remains to be assessed.

Also, in recent years a test particle computer simulation model of the gyroresonant wave-particle interaction in the magnetosphere has been developed and applied for estimating the steady state precipitation fluxes induced by monochromatic VLF signals [*Inan et al.*, 1978]. This model was further extended to include transient behavior and has also been used for calculating the temporal variation and energy spectrum of precipitated flux due to finite duration VLF wave pulses [*Inan et al.*, 1982]. Extension of the model to include relativistic corrections that become necessary at low L values and/or less dense regions of the magnetosphere has led to direct application of the model to the parameters of satellite based particle detector experiments [*Chang and Inan*, 1983].

In this paper, we make use of the extended model in defining the spatial extent of the precipitation zones in the vicinity of major ground based VLF signal sources. In doing so we assume that the signals propagate in the magnetosphere in the field-aligned mode, i.e., in "ducts" of enhanced ionization. The precipitated energy flux as well as the energy of the particles that constitute the flux are computed at 1° steps in longitude and latitude in a ±17° region around the source site. A comparison of various sources shows the importance of the geomagnetic location of the source as well as its operating frequency and radiated power. Some of the results given here were presented earlier in a Stanford University technical report [*Inan*, 1981].

2. DESCRIPTION OF THE WAVE-PARTICLE INTERACTION

Figure 1 depicts the geometry of the wave-particle gyroresonance interaction in the magnetosphere. A ground-based VLF transmitter (T) and two geomagnetic field lines L_1 and L_2, the ionospheric crossings of which are at distances r_1 and r_2 from the transmitter, are shown. The top panel shows the complete field lines, whereas the bottom panel shows an enlarged view of the vicinity of the transmitter.

The circularly polarized wave ($\mathbf{k}$) and the gyrating energetic particles ($v_\parallel$) interact when the doppler-shifted wave frequency as seen by the particles is close to the electron gyrofrequency (f_H). While the particle motion is confined to the magnetic field lines, the ray path for the injected waves are field aligned only under certain conditions. In the magnetosphere, whistler mode waves can propagate in the field-aligned mode in ducts of enhanced ionization [*Helliwell*, 1965]. However, such longitudinal propagation is only possible if $f/f_H < 0.5$, where f is the wave frequency. For

Paper number 4A0121.
0148-0227/84/004A-0121$05.00

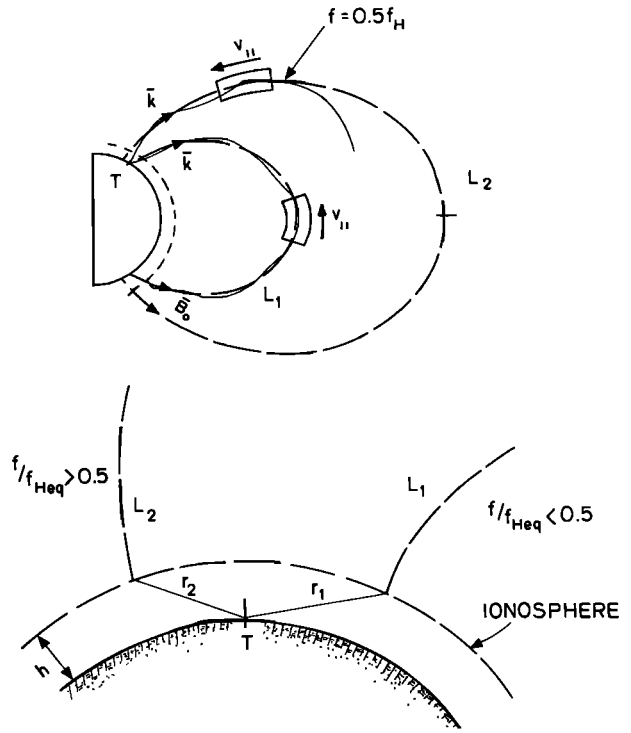

Fig. 1. Description of the wave-particle interaction involving signals from ground based-sources.

$f/f_H > 0.5$, the ray path deviates away from the duct. Although there are other nonducted modes of propagation in which the ray direction may stay closely aligned to the field lines on a portion of the ray path, in such cases the wave normal angle must be nonzero. Longitudinal propagation is also possible in "depletion" ducts for $f/f_H > 0.5$ [*Inan and Bell,* 1977]. In this report we consider only longitudinal wave propagation in which the wave number **k** is approximately parallel to the magnetic field lines and assume that the ray path stays field-aligned only for $f/f_H < 0.5$. The consequences of this assumption are elaborated in the discussion section.

For the earth's magnetic field the electron gyrofrequency is a minimum at the geomagnetic equator. Thus propagation from one hemisphere to another in the field-aligned mode on a given magnetic field line is only possible if $f/f_{Heq} < 0.5$, where f_{Heq} is the equatorial gyrofrequency on that field line. This is the case in Figure 1 for field line L_1, but is not the case for L_2. Hence on L_2 the ray begins to deviate from the field line at the point where $f \simeq f_H/2$. As the wave propagates along the field line it interacts with particles of different energies in the vicinity of points where the cyclotron resonance condition is satisfied. This can be written as

$$f - \frac{kv_{\parallel}}{2\pi} \simeq f_H \tag{1}$$

where $v_{\parallel}$ is the particle velocity. Note that because of the inhomogeneity of the medium k and f_H vary along the field line. For L_1 the strongest interaction occurs around the geomagnetic equator, since that is the region where (1) can be satisfied over the longest distance, assuming a constant wave frequency. Hence the peak of the precipitated flux is due to the interactions in the region shown.

For L_2 the precipitated flux for typical energetic particle distribution functions increases with f/f_H [*Inan et al.,* 1982]. Hence the peak precipitated flux is due mainly to the interaction in the region indicated. In general, however, the precipitated flux due to off-equatorial interactions is less than that due to interactions around the equator, for the same input wave field and on the same field line [*Inan et al.,* 1982]. The relative precipitated flux levels at L_1 and L_2 depend, among other things, on the wave power input into the medium at these L shells. This in turn depends on the distances r_1 and r_2. The determination of the wave power input into the medium is the subject of the next section.

3. Transmitter Signal Intensities in the Magnetosphere

The major portion of the energy radiated by a ground-based VLF transmitter travels in the earth-ionosphere waveguide [*Wait,* 1962]. Calculation of the vertical component of VLF field strengths for a path between two points on the ground have been carried out by *Crary* [1961]. His results indicate that for a wave frequency of 15 kHz, a summer night model ionosphere and for propagation over sea water, the attenuation rate is 20 dB/1000 km for ground points within about 1500 km of the source, and 2 dB/1000 km for distances further away. Although these values were shown to vary with conditions they are nevertheless typical and are used below in our calculations. Using these together with the radiation pattern of the transmitter antenna we have calculated the power density immediately below the ionosphere (at 90 km altitude) as a function of the ground distance from the source point. The radiating elements used by most of the VLF transmitters (except the Siple station transmitter) considered in this report are vertical monopoles of lengths much shorter than a wavelength; hence the radiation pattern is simply taken to be proportional to $\sin^2\theta$ where θ is the angle from the vertical [*Jordan and Balmain,* 1968]. In this case the power density P_d (W/m^2) at 90 km altitude and at a distance r from the transmitter is given by

$$P_d = (3/4)P_T \sin^2\theta/r^2 \tag{2}$$

where P_T is the total power (watts) radiated from the antenna. The P_d given in (2) should be a reasonably good approximation of the actual power density except at grazing angles ($\theta \simeq 0°$) where the radiated power diminishes due to the effects of the imperfect ground [*Wait,* 1962]. For our purposes (2) will be used up to ground distances of roughly 1500 km, beyond which P_d is computed by using the 2 dB/1000 km loss as estimated by *Crary* [1961].

A portion of the energy that is incident on the bottom of the ionosphere can couple into the ionosphere and propagate upward into the magnetosphere. Once the energy is coupled into the magnetoionic medium it can propagate either in field-aligned ducts of enhanced ionization (ducted mode) or in nonducted paths with the ray direction determined by the slowly varying parameters of the medium along the ray path [*Smith et al.,* 1960]. The amount of coupling is determined among other things by absorption in the ionospheric D region, ray coupling into the duct, and the coupling between the two wave polarizations [*Walker,* 1976]. All of these effects are functions of local time, wave frequency, availability of ducts, geographic location, and geomagnetic conditions. The modeling of these is not necessary for the

purposes of our study. Instead, we approach the problem through estimates of a single parameter $K(f, \lambda)$, the proportionality constant between the power density P_d incident on the bottom of the ionosphere, and P_1 the power density inside the magnetosphere at, for example, 1000 km altitude. Thus

$$P_1 = KP_d \tag{3}$$

where K can be obtained from measurements, or estimated theoretically. Note that K is a function of a number of parameters, including frequency f and geomagnetic latitude λ. In this report we only consider the dependence of K on f and λ as explained below.

In order to estimate the wave power density at points higher up along the field line using the P_1 as determined above, one needs to know how the wave power is mapped upward along the field lines. In the general case, this would depend on the distribution of the ray paths and thus indirectly on the cold plasma density distribution. Significant focusing or defocusing of ray paths and thus the wave power density can be expected to occur as a result of relatively small size density irregularities as well as larger size structures such as the plasmapause [*Inan and Bell*, 1977; *Edgar*, 1976]. Relatively common occurrence of such irregularities and the variable nature of the plasmapause location and gradients makes the choice of a specific density profile and ray path distribution rather arbitrary and nongeneral. For this reason, in this paper we choose to map the wave power to higher altitudes assuming ducted propagation of the waves along the geomagnetic field lines. This is also consistent with our assumption of longitudinal wave propagation in the previous section as well as in applying the results of the test particle wave-particle interaction model in the following sections.

According to this, the wave power density P at any point along the field line is obtained by

$$P = \frac{P_1 f_H}{f_{H1}} \tag{4}$$

where f_H and f_{H1} are the electron gyrofrequency locally and at 1000 km, respectively. Once P is obtained , the local wave magnetic field intensity can be found as,

$$B_w = (n/c\mu_0)^{1/2} P^{1/2} \tag{5}$$

where c is the speed of light, μ_0 is the permeability of free space, and n is the local refractive index. Equations (4) and (5) are a result of the slowly varying properties of the medium and the fact that the cross-sectional area of the duct to which the energy is assumed to be confined is proportional to f_H [*Budden*, 1961; *Helliwell*, 1965; *Inan et al.*, 1982].

3.1. Modeling of Ionospheric Losses

For a nighttime ionosphere at midlatitudes and in the frequency range 2–20 kHz, the power loss in the ionosphere between the lower boundary and 1000 km altitude has been estimated by *Helliwell* [1965]. In our formulation we employ the numerical results given in Figure 3.35 of *Helliwell* [1965] for a nighttime ionosphere at 20 kHz as a function of frequency and geomagnetic latitude and use a $\sqrt{f}$ frequency dependence to determine the absorption at other frequencies. Since all of the VLF signal sources considered use linearly polarized antennas, whereas the whistler mode signal is circularly polarized, we add a 3-dB polarization loss to the absorption losses computed as indicated. Thus, we obtain a first estimate of K representing the absorption and polarization losses and neglecting all other factors. At 20 kHz and at $\lambda \simeq 50°$, $K \simeq -7$ dB.

In the rest of the calculations for this report, we employ the K values computed as described above. It should be noted that we consider here a nighttime ionosphere and that the difference between nighttime and daytime absorption within the D region can be as much as 25–30 dB [*Helliwell*, 1965]. Also, in addition to the frequency and latitude dependence of absorption that is accounted for, there exist significant temporal and geographic variations that may need to be considered in a more complete study.

3.2. Comparison With Measurements on the DE-1 Satellite

The K values obtained from the model described above are within 10 dB of those that can be deduced from previously reported direct measurements of transmitter signals on the high-altitude IMP 6 [*Inan et al.*, 1977] and low-altitude OGO 4 [*Scarabucci*, 1969] satellites and are also consistent with rocket observations of upgoing signals from the Siple, Antarctica, VLF transmitter [*Kintner et al.*, 1983].

A comparison of this assumed model for estimating the wave power density that couples into the magnetosphere and a more recent measurement on the Dynamics Explorer 1 (DE-1) satellite is given in Figure 2. The scattered points are direct measurements of the wave magnetic field intensity on the DE-1 satellite during its pass over the Omega, North Dakota, navigation transmitter on January 11, 1982. During this particular pass the satellite longitude was within $\pm 2°$ in longitude of that of the source and moved in latitude (L) as given in Figure 2 at an altitude that varied from ~ 2500 to 6000 km. The data were acquired by using the Stanford University Linear Wave Receiver (LWR) on DE-1 [*Inan and Helliwell*, 1982; *Shawhan et al.*, 1981]. A loop antenna was used to acquire broadband wave data in the 10–16 kHz range. The wave magnetic field intensity in a 100 Hz band around 13.1 kHz was then estimated by using the receiver calibration references.

The solid line in this figure shows B_w, the computed field intensity at the satellite altitude, plotted as a function of L value (geomagnetic latitude) at the longitude of the Omega, North Dakota, transmitter (see Table 1). The transmitter has a radiated power of 10 kW and utilizes 0.9- to 1.2-s pulses at frequencies in the range 10.2–13.6 kHz. Since the highest duty cycle is at 13.1 kHz we have made our calculations and measurement at this frequency. We have used the model described above for computing P_1, except for an additional 26 dB absorption due to the day/night difference [*Helliwell*, 1965] (the satellite pass occurred during local daylight conditions). In order to convert P_1 to B_w at the satellite altitude through (4) and (5) we have used a Jensen and Cain model of the earth's magnetic field [*Jensen and Cain*, 1962] and a diffusive equilibrium model of the magnetospheric cold plasma distribution with the equatorial density N_{eq} as given in Figure 3 [*Angerami and Thomas*, 1964].

Figure 2 shows that the computed variation of B_w with L as well as the absolute field intensity agree well with the observations, especially in view of the simplicity of the model and the temporal and geographic variations of ionospheric

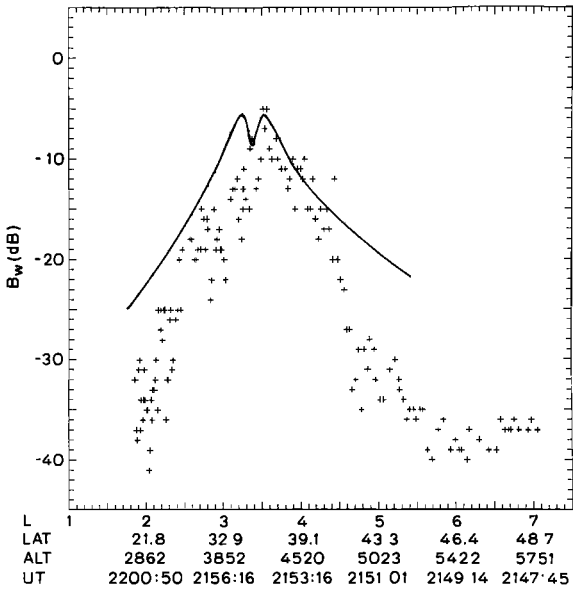

Fig. 2. Comparison of the computed and observed values of B_w, with 0 dB corresponding to $B_w = 0.86$ pT. The points represent the absolute wave magnetic field intensity observed on January 11, 1982 with the Linear Wave Receiver (LWR) on the DE-1 satellite. The coordinates of the satellite in geographic latitude and altitude (km) as well as UT are given on the abcissa. The solid line represents the B_w computed by using the model described in the text for the ionospheric losses and equations (2), (3), and (4). For the variation of the refractive index n, a diffusive equilibrium model for the electron density with an equatorial density profile as given in Figure 3 is used.

absorption that are not considered [*Helliwell,* 1965]. Also, as shown in (5) above, the field intensity B_w is proportional to $N_e^{1/4}$, where N_e is the local cold plasma density obtained by using a diffusive equilibrium model and the equatorial variation of N_e as given in Figure 3. Since the N_{eq} versus L profile at the time of the measurements would be expected to be different than the sample typical profile of Figure 3, some discrepancy between the measured and computed values of B_w is to be expected. Indeed, statistical evidence shows that during local winter conditions the densities in the range $2 < L < 3$ can be expected to be higher than those of Figure 2 by a factor $\sim$5–10 [*Park et al.,* 1978]. At higher latitudes the density values are more variable with magnetospheric conditions, depending on the plasmapause location, gradients, and geomagnetic activity. Thus, the more rapid decrease of the observed B_w values with increasing L for $L > 4$ is probably an indication of a relatively sharper drop in density (i.e, a plasmapause)at $\sim$4.5 than that shown in Figure 3. In this sense, the observed variation of B_w with L constitutes a measure of the plasmapause location. The observed field intensity at $L = 5$ is $\sim$10 dB below the computed one indicating that the density at that L value may be smaller by a factor of $\sim$100 than that shown in Figure 3. This would give a density $N_{eq} = 2$ el/cc at $L = 5$, which is in the range of typical density levels (1–10 el/cc) at this L value outside the plasmapause [*Park et al.,* 1978].

It should be noted here that the comparison of Figure 2 is not intended as a justification of the ducted propagation assumption that is used in mapping the wave power density along the field lines using (4) and (5). In fact, this would not be possible since the maximum satellite altitude for the case shown was $\sim$6000 km, well below the equatorial region in the vicinity of which most of the wave-induced pitch angle scattering occurs [*Inan et al.,* 1982] and therefore at which point the local B_w value becomes critical in terms of determining the precipitated flux. Rather, our motivation in showing the result in Figure 2 is to confirm and justify the computation of the absolute wave power density P_1 by using the radiated power of the transmitter, modeling the subionospheric losses and the coupling losses through the lower ionosphere. For this purpose the relatively low altitude observations shown in Figure 2 are particulary suitable, for while the signals observed on DE-1 were probably propagating in the nonducted mode, the spreading loss for the ducted and nonducted cases between 1000 km and $\sim$2500–6000 km altitude would not be too different. In terms of determining the equatorial wave magnetic field intensity, the ducted model used in this paper remains a convenient assumption, not to be representative of the general case but as a good illustrative example. This is especially true since the ray path distribution and thus the upward mapping of the wave power density in specific cases would be strongly dependent on the details of the background cold plasma density profile which itself is quite variable. This point is further stated in the discussion section below.

3.3. Existing VLF Transmitters

In Table 1 we list some of the major ground based VLF transmitters that are currently in operation [*ITU,* 1979]. Most of this information presented is contained in the reference given, although some additions have been made on the basis of observations at ground-based VLF stations. The radiated power levels can, for instance, be verified by comparing observed field intensities of different stations and incorporating the ionospheric propagation losses over the path from the source to the receiver [*Inan and Helliwell,* 1982]. Other than the experimental transmitter located at Siple station, Antarctica, we have listed in Table 1 only those VLF transmitters that operate at radiated power levels >10 kW.

The equatorial magnetic field intensities for some of these VLF transmitters, estimated by using the model described above, are given in Table 2. The columns in the table contain the L value of the magnetic field line, the ratio of wave frequency to the equatorial gyrofrequency on that field line, the ground distance between the foot of the field line and the transmitter location (at the geomag-

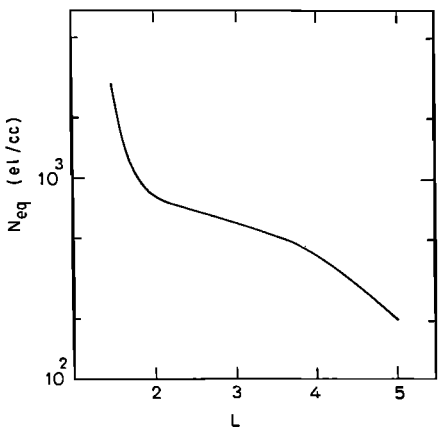

Fig. 3. The equatorial cold plasma density profile used for the calculations in this paper. A diffusive equilibrium model is used for the variation of the density along the field lines.

TABLE 1. List of Major VLF Transmitters

Transmitters	Latitude (deg)	Longitude (deg)	Radiated Power (kW)	Frequency (kHz)
Communication Transmitters				
NAA (Cutler, Maine)	44°39'N	67°17'N	1000	17.8
NLK (Jim Creek, Washington)	48°12'N	121°55'W	850	24.8
NPM (Lualuaiei, Hawaii)	21°25'N	158°09'W	300	23.4
NSS (Annapolis, Maryland)	38°59'N	76°27'W	265	21.4
NWC (N. W. Cape, Australia)	21°49'S	114°10'E	1000	22.3
GBR (Great Britain)	52°20'N	00°20'W	300	16.0
UMS* (Gorki, USSR)	56°N	44°E	~1000	16.2
RPS* (Eastern Siberia, USSR)	43°N	135°E	~1000	17.1
Navigation Transmitters				
Omega A (Norway)	66°25'N	13°08'E	10	10.2–13.6
Omega B (Liberia)	06°18'N	10°89'W	10	10.2–13.6
Omega C (Hawaii)	21°24'N	157°49'W	10	10.2–13.6
Omega D (North Dakota)	46°21'N	98°29'W	10	10.2–13.6
Omega E (La Reunion)	20°58'N	55°17'E	10	10.2–13.6
Omega F (Argentina)	43°03'S	65°11'W	10	10.2–13.6
Omega G (Trinidad)	10°42'N	61°38'W	10	10.2–13.6
Omega H (Japan)	34°36'N	129°27'E	10	10.2–13.6
Komsomolskamur (USSR)	50°34'N	136°58'E	10–500	11.9–15.6†
Novosibirsk (USSR)	55°04'N	80°58'E	10–500	11.9–15.6
Krasnodar (USSR)	45°02'N	38°39'E	10–500	11.9–15.6
Experimental Transmitter				
SIPLE (Siple, Antarctica)	75°56'S	84°14'W	~3	1–20

*UMS and RPS occasionally interchange call signs and frequency.
† Some specific frequencies are 11.905, 12.5, 12.649, 13.281, 14.881 and 15.625 kHz.

netic longitude of the transmitter), the power density P_d (W/m^2) incident on the bottom of the ionosphere as computed from (2), and the wave magnetic field intensity (pT) at the geomagnetic equator on the field line estimated from (5) for cases where $f/f_{Heq} < 0.5$. In using (4) and (5) the whistler mode refractive index is computed by using a *Jensen and Cain* [1962] model of the earth's magnetic field and a diffusive equilibrium model of the magnetospheric cold plasma [*Angerami and Thomas*, 1964]. The equatorial cold plasma density that was used is shown in Figure 3.

In the next section, we use the estimated wave intensities to deduce the precipitated energy fluxes as a function of distance from the transmitter.

4. The Spatial Distribution of the Precipitation Zones

Once the VLF wave energy enters the magnetosphere it propagates in the whistler mode either inside field-aligned ducts of enhanced ionization (ducted mode) or along ray paths determined by the slowly varying gradients of the inhomogeneous magnetosphere (nonducted mode). In this report we consider only field-aligned propagation. As discussed in the introduction, in this mode the injected signals may travel from one hemisphere to another if $f/f_{Heq} < 0.5$, where f_{Heq} is the equatorial gyrofrequency. In the following, we use $\Lambda = f/f_{Heq}$ for convenience.

For a given ground-based VLF source, the intensity of the signal injected into the medium at any point in the lower ionosphere located a given distance r from the source can be estimated as described in the previous section. Using a dipole magnetic field model, that same point can also be identified with the L value of the magnetic field line that passes through it, and thus a Λ value, since the source frequency is known.

The precipitation flux induced by the injected signal is a complicated function of wave intensity, normalized frequency Λ, cold plasma density, resonant electron energy, energetic particle distribution function, and the field line of propagation (L). In past work a test particle computer simulation of the cyclotron resonance interaction between the wave and the energetic particles has been used to compute the wave flux induced [*Inan et al.*, 1978; 1982]. Separate calculations for the parameters of different transmitters are not required at the level of the present study, since we may utilize some recent results obtained by *Inan et al.* [1982] for estimating the wave-induced precipitation fluxes.

Using a model magnetosphere, *Inan et al.* [1982] computed the precipitated energy fluxes for normalized frequencies $\Lambda = 0.5, 0.1, 0.25, 0.5, 0.75, 1, 2$, and for field lines $L = 1.5, 2, 3, 4, 5$, as given in Figure 17 of that paper.

TABLE 2. Equatorial Magnetic Field Intensities

Latitude (deg)	L	f/f_{Heq}	Distance (km)	P_d (W/m^2)	B_ω (pT)
NAA [a]					
34.	2.18	0.21	1182.	0.17E–06	5.8
36.	2.34	0.26	960.	0.25E–06	7.0
38.	2.53	0.33	739.	0.42E–06	8.9
40.	2.75	0.43	518.	0.83E–06	12.4
42.	3.01	0.56	299.	0.22E–05	
44.	3.32	0.74	92.	0.73E–05	
46.	3.38	1.01	159.	0.54E–05	
48.	4.11	1.41	375.	0.15E–05	
50.	4.63	2.02	595.	0.64E–06	
52.	5.26	2.97	816.	0.35E–06	
NLK [b]					
38.	1.88	0.19	1163.	0.15E–06	5.4
40.	2.02	0.23	942.	0.22E–06	6.6
42.	2.18	0.29	720.	0.38E–06	3.4
44.	2.37	0.38	498.	0.76E–06	11.8
46.	2.59	0.49	277.	0.22E–05	19.9
48.	2.84	0.65	55.	0.50E–05	
50.	3.14	0.88	166.	0.44E–05	
52.	3.51	1.22	388.	0.12E–05	
54.	3.94	1.74	609.	0.52E–05	
56.	4.47	2.53	831.	0.29E–06	
NSS [c]					
32.	2.02	0.20	722.	0.12E–06	4.3
34.	2.17	0.25	501.	0.24E–06	6.0
36.	2.34	0.31	281.	0.66E–06	10.0
38.	2.54	0.40	73.	0.19E–05	16.9
40.	2.78	0.52	172.	0.13E–05	
42.	3.05	0.70	390.	0.37E–06	
44.	3.37	0.94	611.	0.16E–06	
46.	3.76	1.30	832.	0.89E–07	
48.	4.22	1.84	1053.	0.56E–07	
50.	4.78	2.68	1275.	0.38E–07	
NDK [d]					
36.	2.08	0.13	1147.	0.18E–08	0.8
38.	2.26	0.17	926.	0.27E–08	0.9
40.	2.46	0.22	704.	0.46E–08	1.1
42.	2.70	0.30	483.	0.95E–08	1.6
44.	2.99	0.40	263.	0.28E–07	2.6
46.	3.32	0.55	53.	0.57E–07	
48.	3.73	0.78	186.	0.45E–07	
50.	4.22	1.12	406.	0.13E–07	
52.	4.81	1.67	627.	0.58E–08	
54.	5.55	2.56	848.	0.32E–08	
SIPLE [e]					
-79.	5.12	0.77	332.	0.40E–08	
-77.	4.49	0.52	110.	0.23E–07	
-75.	3.97	0.36	110.	0.23E–07	3.4
-73.	3.55	0.26	332.	0.40E–08	1.5
-71.	3.20	0.19	554.	0.15E–08	1.0
-69.	2.90	0.14	775.	0.78E–09	0.8
-67.	2.65	0.11	997.	0.48E–09	0.7
-65.	2.44	0.08	1219.	0.32E–09	0.6
-63.	2.26	0.07	1440.	0.23E–09	0.5
-61.	2.11	0.05	1662.	0.20E–09	0.5

TABLE 2. Continued

Latitude (deg)	L	f/f_{Heq}	Distance (km)	P_d (W/m^2)	B_ω (pT)
KOM [f]					
53.	2.02	0.11	269.	0.13E–05	30.5
55.	2.19	0.14	491.	0.46E–06	17.0
57.	2.39	0.18	712.	0.23E–06	11.3
59.	2.61	0.24	934.	0.13E–06	8.1
61.	2.88	0.33	1156.	0.88E–07	6.2
63.	3.20	0.45	1377.	0.62E–07	4.9
65.	3.59	0.63	1599.	0.50E–07	
67.	4.05	0.90	1821.	0.45E–07	
69.	4.61	1.34	2042.	0.41E–07	
71.	5.31	2.04	2264.	0.37E–07	
UMS [g]					
51.	2.09	0.17	554.	0.74E–06	18.4
53.	2.27	0.22	332.	0.19E–05	28.1
55.	2.47	0.28	110.	0.70E–05	52.2
57.	2.70	0.37	110.	0.70E–05	50.1
59.	2.98	0.49	332.	0.19E–05	25.1
61.	3.30	0.67	554.	0.74E–06	
63.	3.68	0.93	775.	0.38E–06	
65.	4.14	1.32	997.	0.24E–06	
67.	4.69	1.92	1219.	0.16E–06	
69.	5.37	2.87	1440.	0.11E–06	

[a] *Cutler, Maine*, $L = 3.42$, 17.8 kHz, 1000 kW.
[b] *Jim Creek, Washington*, $L = 2.92$, 24.8 kHz, 850 kW.
[c] *Annapolis, Maryland*, $L = 2.60$, 21.4 kHz, 265 kW.
[d] *Omega, North Dakota*, $L = 3.37$, 13.1 kHz, 10 kW.
[e] *Siple Station, Antarctica*, $L = 4.22$, 5.0 kHz, 3 kW.
[f] *Konsomolskamur, USSR*, $L = 1.85$, 11.9 kHz, 500 kW.
[g] *Gorki, USSR*, $L = 2.58$, 16.2 kHz, 1000 kW.

For our purpose, we have renormalized these for $B_\omega = 1$ pT intensity at 1000 km altitude and have added relativistic corrections using a more recent extension of the model [*Chang and Inan*, 1983]. Figure 4 shows normalized peak energy flux as a function of Λ, parametric in L value and for a diffusive equilibrium model of the cold plasma with the equatorial density as given in Figure 3. The distribution of the energetic particles for this case was assumed to be the same at all L values, with $f(v, \alpha) = Av^{-6}$, where v and α are the velocity and pitch angle of the particles, respectively, and A is a proportionality constant. The ordinate values in Figure 4 represent normalized units. In order to convert these to energy flux in ergs/cm^2 s, the normalized values need to be multiplied by $10^{-8}\Phi_1$, where Φ_1 is the differential energy spectrum of the trapped particles in units of el/cm^2 s sr keV for 1-keV electrons at 90° pitch angle (for an isotropic distribution as is assumed here, this would be the trapped flux level near the edge of the loss cone).

The peak fluxes given in Figure 4 are in general composed of particles having a range of energies, with most of the contribution coming from the lower end of the range. The minimum energy of the particles that constitute the peak fluxes of Figure 4 are shown in Figure 5 (Figure 21 of *Inan et al.* [1982]).

With L, B_w, and Λ determined, the flux induced by the signal that enters the medium at a given point can be ap-

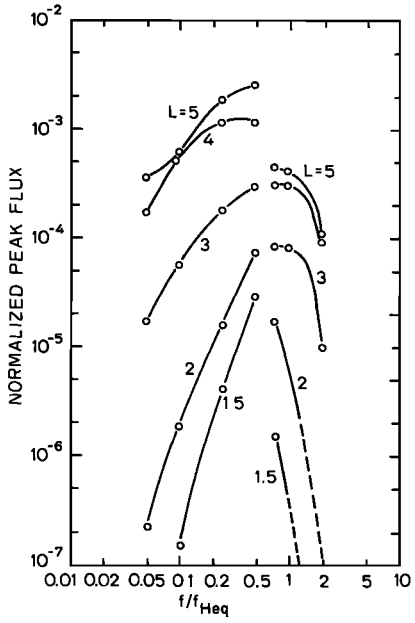

Fig. 4. Normalized peak energy flux as a function of normalized frequency Λ for L=1.5, 2, 3, 4, and 5. The peak fluxes given are normalized to a wave magnetic field intensity of B_w=1 pT at 1000 km altitude [*Inan et al.*, 1982]. The energetic particle distribution $f(v, \alpha)$ was assumed to be proportional to v^{-6}, where v is the particle velocity. The normalized abcissa values can be converted to energy flux in ergs/cm^2 s by multiplying with $10^{-8}\Phi_1$, where Φ_1 is the differential energy spectrum of the trapped particles in units of el/cm^2 s sr keV for 1-keV electrons near the edge of the loss cone.

proximately determined by interpolation between the values given in Figure 4, if it can be assumed that the precipitated flux is linearly proportional to the wave intensity. It has been shown that at $L = 4$ this is valid for B_w less than 10 pT [*Inan et al.*, 1982], at lower L values the assumption can be safely made for even higher values of B_w (see Figure 14*b* of *Inan et al.* [1982]). Furthermore, recent measurements of whistler precipitation induced amplitude perturbations of subionospherically propagating VLF signals have shown that the percentage perturbation is linearly related to the intensity of the perturbing whistler [*Carpenter and LaBelle*, 1982]. Since in most cases the wave intensities of interest are not much higher than the equivalent of 10 pT at L =4, in our formulation we have assumed a linear dependence of the precipitated flux on B_w.

We now consider the application of this procedure to the cases of some major VLF transmitters.

4.1. NAA Transmitter in Cutler, Maine

As can be seen in Table 1, The U. S. Navy communication transmitter NAA located at Cutler, Maine (44°39′N, 67°17′W), has a radiated power of 1000 kW and an operating frequency of 17.8 kHz. Figure 6*a* shows a plot of peak precipitated energy flux as a function of geographic latitude at the longitude of NAA. Figure 6*b*, on the other hand, shows the flux as a function of geographic longitude at the transmitter latitude. The flux values were previously determined at discrete values of Λ and L (Figure 4), and we have used a two-dimensional linear interpolation scheme to find the flux for any arbitrary pair of values of Λ and L.

The minimum energy of the particles that constitute the peak fluxes is shown as a function of latitude (at the transmitter longitude) in Figure 7*a* and longitude (at the transmitter latitude) in Figure 7*b*. Although the contributions to the peak flux come from a range of particle energies, only the minimum energy is shown, since in most cases the maximum contribution to the flux comes from the lowest energy particles [*Inan et al.*, 1982]. These values were obtained by interpolating between the ones given in Figure 5.

Note from Figures 6*a* and 7*a* that the flux and the particle energy change rather abruptly at $\sim$47.5° latitude. This can be understood by careful examination of Figure 4, which shows that for each L value, the flux drops relatively abruptly between Λ = 0.5 and 0.75. This in turn is due to the fact that for $\Lambda > 0.5$ the wave signal is assumed not to cross the equator, thus eliminating the contributions to the peak flux due to the particles that resonate with the wave after it crosses the equator [*Inan et al.*, 1982]. The temporal shape of the precipitation pulse therefore changes, thus changing the identification of the peak flux point [*Inan et al.*, 1982]. Note that the flux values of Figure 6*a* are obtained by using a two-dimensional interpolation scheme as described above; thus for a fixed wave frequency such as f = 17.8 kHz the flux values can be read along the locus of the points that correspond to the values of Λ for a given L (f_{Heq}). As an artifact of this interpolation, there exists two discontinuities in the rate of change of flux with L, one at Λ = 0.5 and the other at Λ = 0.75. This is the source of the apparent discontinuities (inflection points) in the figures 6*a*, 7*a*, 7*b*, 9*b*, 10*b*, 11*b*, 12*b*, 13*b*, and 14*b*.

The longitude variation of flux shown in Figure 6*b* is comparatively slow. At the longitude of the NAA Transmitter the constant geomagnetic and geographic latitude lines are almost parallel to each other; thus, the main reason for the flux variation shown is the decrease in B_w with distance from the source in accordance with (4). The relatively slow variation of energy with longitude shown in Figure 7*b* can be understood in the same way, since the energy of the downcoming particles is determined by the cold plasma model employed (Figure 3) , Λ and L.

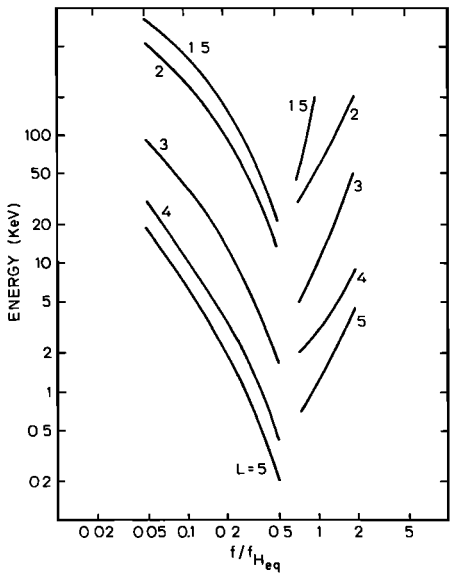

Fig. 5. The minumum energy of particles that constitute the fluxes given in Figure 4, given as function of Λ for various values of L.

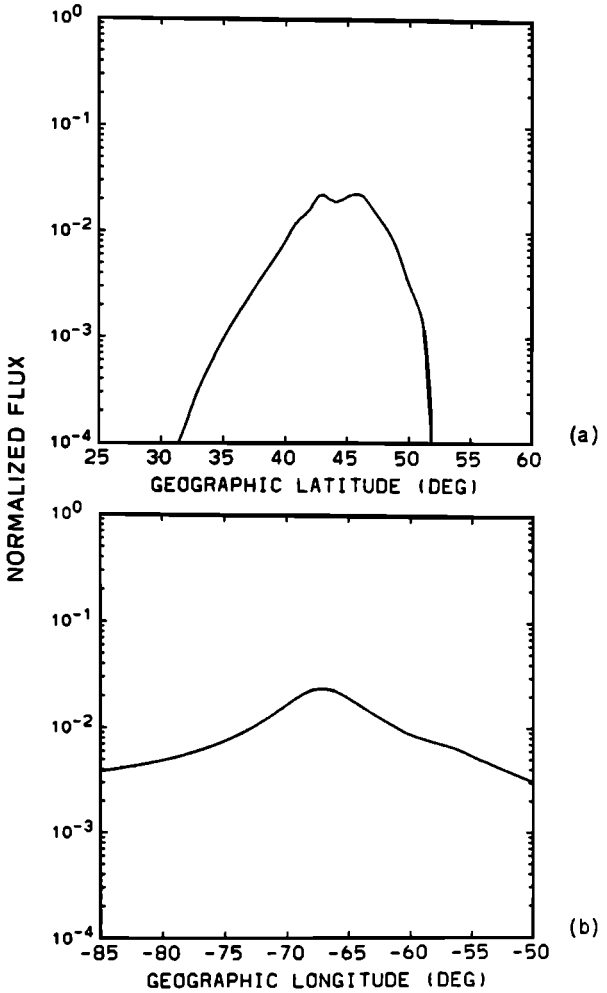

Fig. 6. Normalized precipitated energy flux for the NAA transmitter as a function of latitude and longitude respectively, at the longitude and the latitude of the source.

In order to display the spatial distribution of the precipitated energy, we consider a region covering roughly $\pm 17^\circ$ in longitude and latitude around the transmitter site. In this region, we take mesh points spaced by 1° in latitude and longitude. For each of the mesh points, L, Λ, and B_w can be determined from the given transmitter frequency (f), geographic location, and radiated power (P_T) as discussed above. The peak precipitated flux for each injection point is then estimated by interpolating between the values of Figure 4 and scaling with B_w. For our purposes it is assumed that the whistler mode signal propagates along the same field line, so that the field line of propagation has the same L value as that of the injection point. Hence, the downcoming flux due to a wave injected at a given L is assumed to be precipitated at the same location. In the context of ducted propagations, this is equivalent to assuming that the duct extends down to the lower ionosphere.

We have developed a computer code that carries out the calculations described above. The inputs to the program are f, P_T, geographic location (latitude,longitude) of the source, and the data of Figures 4 and 5. The program uses a Jensen and Cain model of the earth's magnetic field [*Jensen and Cain*, 1962] to estimate the L value corresponding to a given point on the globe. The calculations of the equatorial gyrofrequency and thus Λ are made by assuming a dipole model for the magnetic field. The output is a contour plot of the peak energy flux on a section of a map showing the vicinity ($\pm 17^\circ$ in latitude and longitude) of the transmitter. The result for the NAA transmitter is shown in Figure 8a. Also shown are the locii of the $L = 2$, 3, 4, and 5 field lines. The projection used for the map is the cylindrical equidistant projection which allows for the mapping of the entire globe on a plane. The numbers on the contours, when multiplied by $10^{-10}\Phi_1$ give the energy flux in ergs/cm^2 s, where Φ_1 is the differential energy spectrum of 1-keV electrons near the edge of the loss cone in units of el/cm^2 s sr keV. The energetic particle distribution function is assumed to be proportional to v^{-6}, as in the case for of the results given in Figure 4 [*Inan et al.*, 1982]. This and other assumptions, such as a constant Φ_1 with L, the variation of N_{eq} with L as given by Figure 3 and the availability of ducts, would affect the shape of the precipitation zone. These are discussed in section 5.

Figure 8*b* shows the precipitation zone around the point that is geomagnetically conjugate to the NAA Transmitter. This represents precipitation flux that would be due to a VLF signal that propagates to the conjugate hemisphere and is then reflected. As the reflected signal propagates back to the source hemisphere, it scatters particles that are

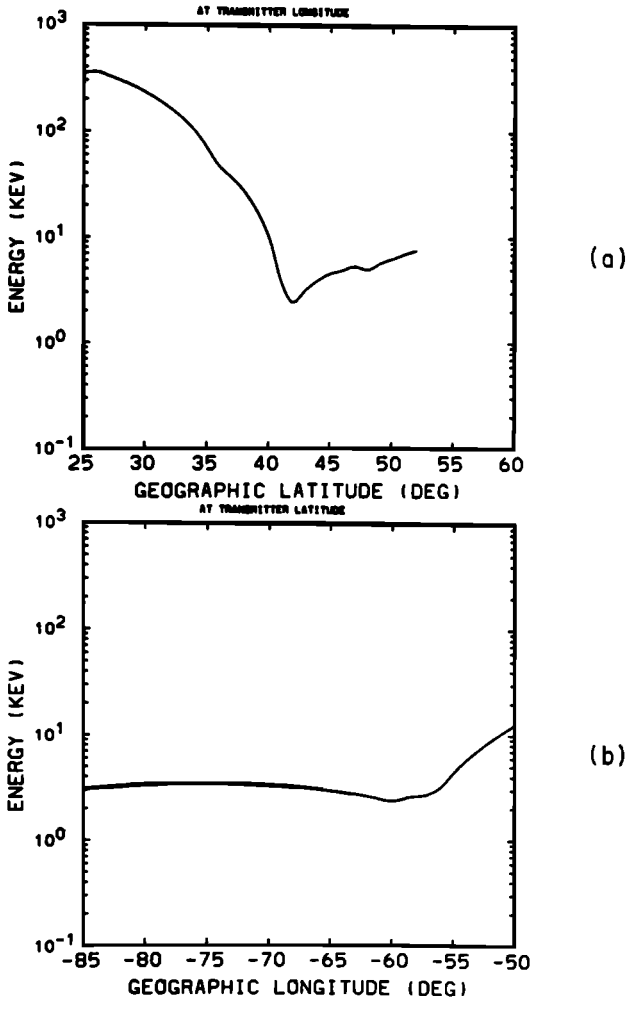

Fig. 7. Minumum energy of the electrons that constitute the fluxes shown in Figure 6.

precipitated in the conjugate hemisphere. In the ducted propagation model assumed here, the whistler mode signal can stay ducted and cross the equator (and therefore reach the conjugate hemisphere) on those field lines for which $\Lambda < 0.5$. The result given in Figure 8*b* takes this into account, since only contributions for $\Lambda < 0.5$ are considered. As a consequence there is a sharp boundary of the zone at $L \simeq 3$.

Note that precipitation onto the region conjugate to the source can also occur owing to the atmospheric backscatter and asymmetric mirroring of particles that were scattered by the direct wave signal [*Walt et al.*, 1968]. This should be especially important at longitudes near the south atlantic anomaly, since in that longitude range there exist significant differences in the mirror heights corresponding to the two hemispheres [*Barish and Wiley*, 1970]. In such a case, the contributions would not be limited to field lines for which $\Lambda < 0.5$ and the precipitation zone shown would then be somewhat wider (at higher latitudes) than that shown in Figure 8*b*.

Owing to the projection used, the distance scale in Figure 8 is distorted, especially at higher latitudes. At any given geographic latitude λ_g, the distance is given by $111.18 \cos \lambda_g$ kilometers per degree geographic longitude.

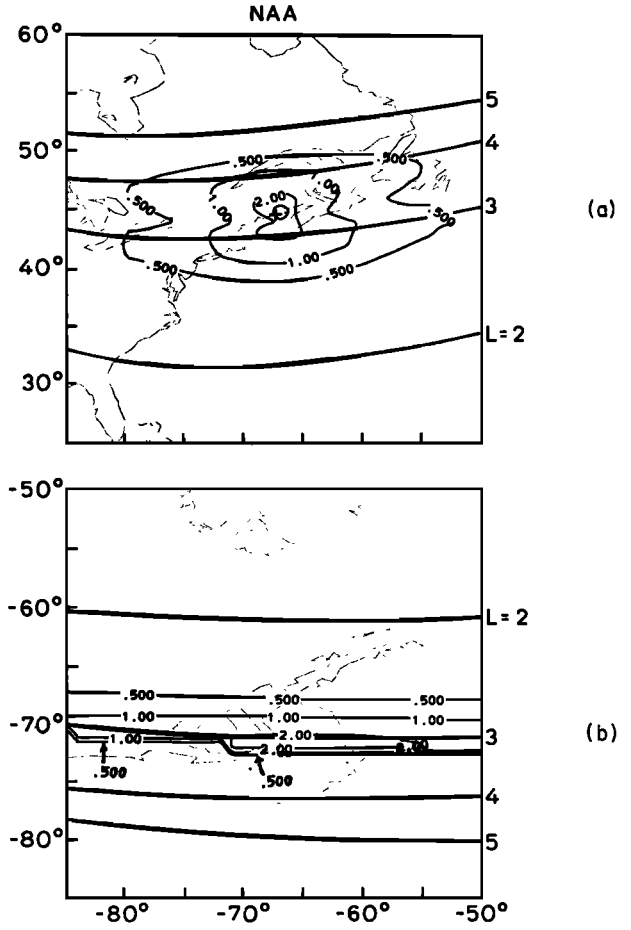

Fig. 8. Precipitation zone around the NAA transmitter and the congate location. The numbers on the contours represent normalized energy flux. The normalized values, when multiplied by $10^{-10}\Phi_1$, can be converted to energy flux in ergs/cm^2 s, where Φ_1 is the differential energy spectrum of 1-keV electrons near the edge of the loss cone in units of el/cm^2 s sr keV.

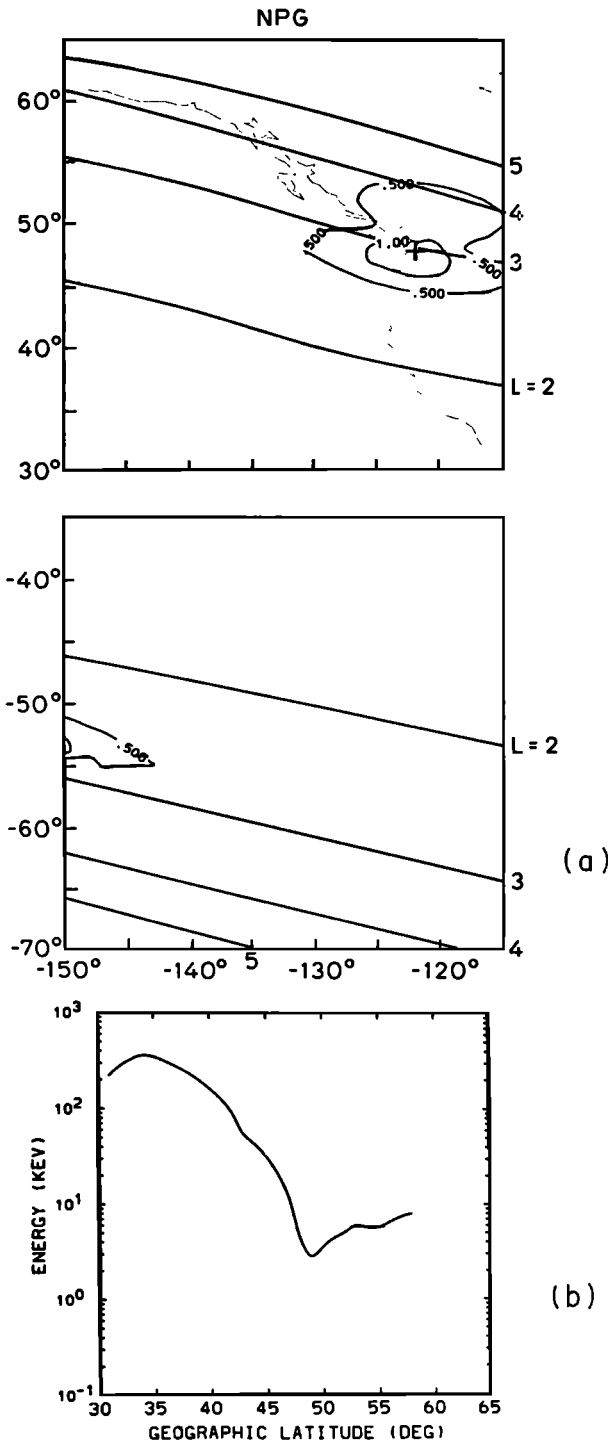

Fig. 9. Precipitation zone around the NPG(NLK) transmitter operating at f=24.8 kHz and with P_T=850 kW and its conjugate location. The format is the same as in Figure 8.

Thus, the widest portions of the two zones shown in Figures 8*a* and 8*b* are both about $\sim$2000 km.

4.2. NLK(NPG) Transmitter in Jim Creek, Washington

Figure 9a shows the precipitation zones around the NLK(NPG) transmitter and its conjugate location. This transmitter operates at 24.8 kHz and has a radiated power of 850 kW. All other parameters have been taken to be the same as for the NAA transmitter. The smaller precipita-

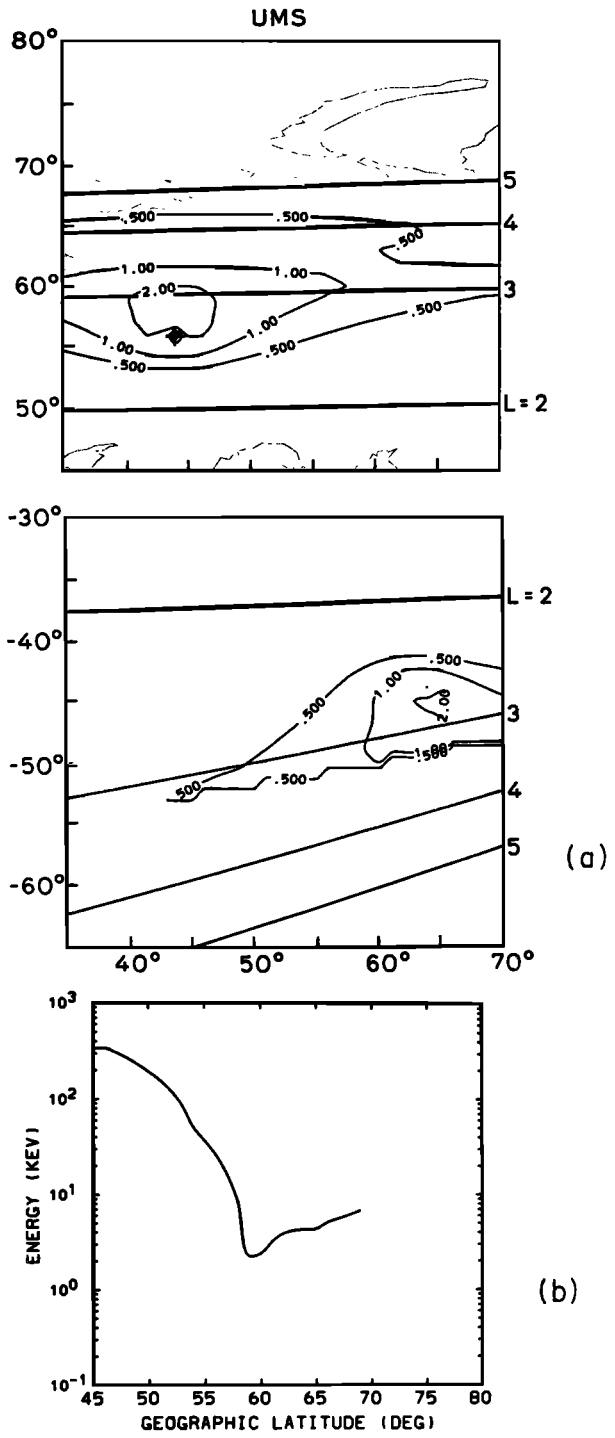

Fig. 10. Precipitation zone around the UMS transmitter operating at f=16.2 kHz and with an assumed P_T=1000 kW and its conjugate location. The format is the same as that of Figure 8.

tion zone for this transmitter with respect to that of NAA illustrates the dependence on the signal frequency, as expected form the result of Figure 4. This result also clearly shows the tendency for the precipitation zones to be aligned with the lines of constant L. This is a result of the fact that the L dependence of the scattering efficiency is dominant over the decrease of input wave intensity as a function of distance from the source. This was also discussed in connection with Figure 6.

The minimum energy of the particles that contribute to the precipitation around the NLK transmitter is shown in Figure 9*b*. The format of this figure is the same as that of Figure 8*b*.

4.3. UMS Transmitter in Gorki, USSR

Figure 10*a* and 10*b* show the precipitation zone and precipitated particle energy respectively around a transmit-

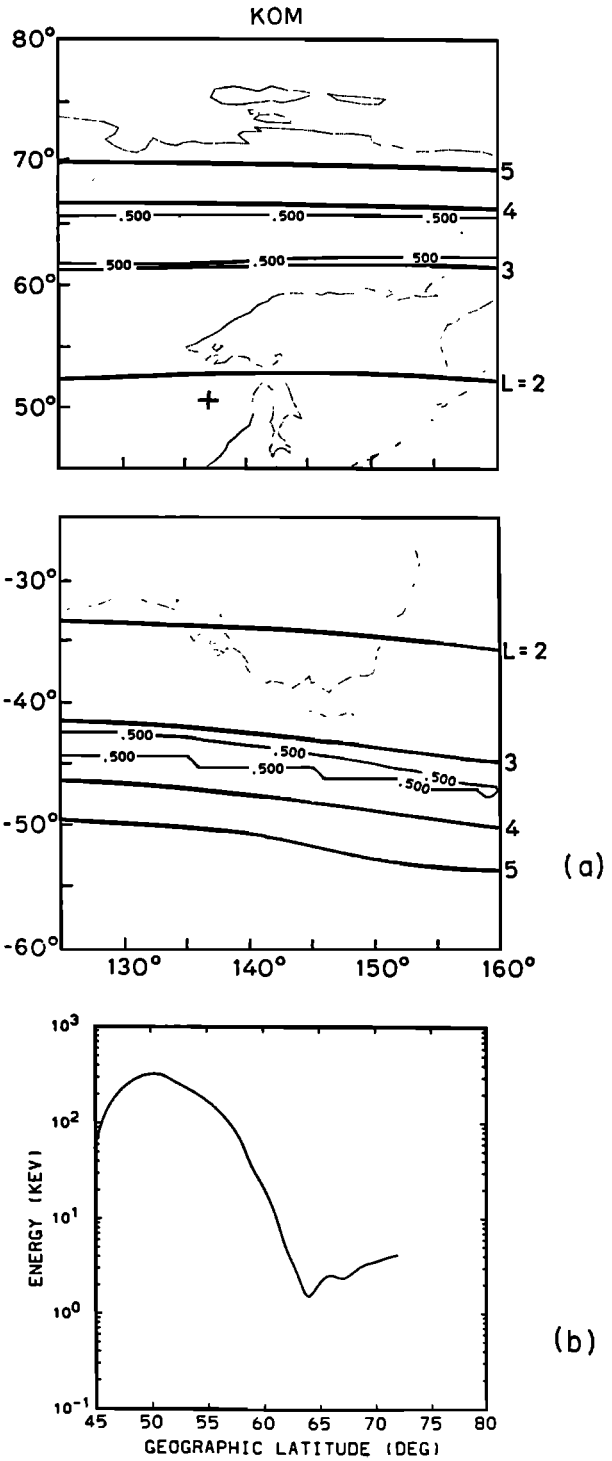

Fig. 11. Precipitation zone around the USSR navigational transmitter at Komsomolskamur, operating at f=11.9 kHz and with P_T=500 kW, and its conjugate location. The format is the same as in Figure 8.

ter located in Gorki, USSR using the call sign UMS. This transmitter operates at 16.2 kHz and at a radiated power of ≃1000 kW (see Table 1). Although the frequency and radiated power level are similar to that of NAA transmitter, this source is located at a lower L value ($L \simeq 2.5$). As a result, the shape of the precipitation zone is quite different. This is again due to the strong L dependence of the precipitation flux evident in Figure 4.

4.4. *Alpha Transmitter in Komsomolskamur, USSR*

Next we consider a VLF navigation transmitter operating at relatively lower (<15 kHz) frequencies and located in the eastern USSR (see Table 1). This transmitter utilizes a format of 0.4-s long pulses at frequencies of 11.88, 12.64, and 14.88 kHz and has a radiated power of 500 kW. DE-1 satellite observations have shown that signals from this transmitter are on occasion amplified and trigger VLF emissions [*Inan and Helliwell,* 1982].

The precipitation zones shown in Figure 11a for this source and for a frequency f=11.88 kHz illustrate the importance of the geomagnetic location of the source as well as the operating frequency. Even though the radiated power is relatively high, the maximum precipitation region is far to the north of the source site, with negligible flux precipitated overhead the transmitter. This again is due to the fact that because of the increased inhomogeneity of the field lines , the precipitation efficiency for given B_w and f decreases rapidly with decreasing L (Figure 4). Thus although this transmitter is located at $L \simeq 1.8$, the maximum precipitation is in the $L \simeq 3$–4 range, where the decrease in B_w with distance from the source is balanced by the increase in flux with L.

A comparison of Figures 11 and 8 shows that even though the Komsomolskamur transmitter radiates only half as much power as NAA and is located at $L \simeq 1.8$, far away from the peak flux region, the sizes of the zones represented by for example the contours marked 0.5 are about the same in Figures 11 and 8. This result is due to the lower frequency of the former transmitter (11.88 versus 17.8 kHz). The lower frequency signals can cross the equator ($\Lambda < 0.5$) on higher L shells and can therefore precipitate higher electron fluxes (see Figure 4) [*Inan et al.,* 1982].

4.5. *NSS Transmitter in Annapolis, Maryland*

Figure 12 shows the precipitation zones around the NSS transmitter and its conjugate point. This transmitter operates at 21.4 kHz and has a radiated power of ~265 kW. All other parameters are taken to be the same as that for the NAA transmitter. The smaller precipitation zone is a combined result of the lower radiated power and the low-latitude (low L) location of this transmitter as compared to NAA. Being very close in longitude to that of NAA, the result for this transmitter does not convey any new features of the spatial distribution of precipitation zones around ground based VLF sources and is shown here mainly for completion.

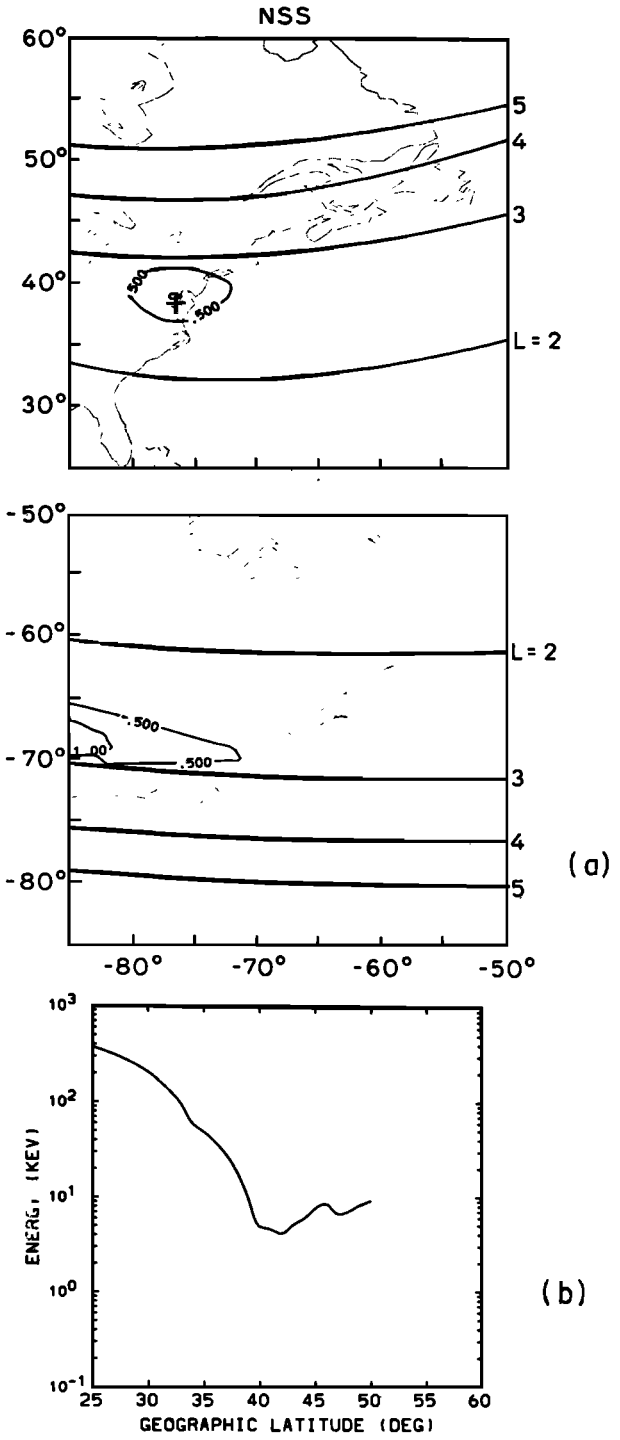

Fig. 12. Precipitation zone around the NSS transmitter, operating at f=21.4 kHz and with P_T=265 kW and its conjugate point. The format is the same as in Figure 8.

4.6. *Omega Transmitter in North Dakota*

The VLF signal sources considered until now were all relatively high-power (>500 kW radiated) transmitters. In Figure 13*a* we show the precipitation zones around the Omega Navigation transmitter located in North Dakota, USA. This source has a radiated power of ≃ 10kW and transmits a specific format consisting of 0.9- to 1.2-s long pulses in the 10.2- to 13.6-kHz range [*Bell et al.,* 1981]. It is one of nine similar Omega transmitters located around the globe (see Table 1). Satellite measurements of the signal intensity of waves from this transmitter were discussed in Figure 2.

For the case shown in Figure 13 we have used a frequency of 13.1 kHz. Although the conjugate precipitation zone seems larger, this is an artifact of the particular type of projection used; for example, the longitudinal spread of the

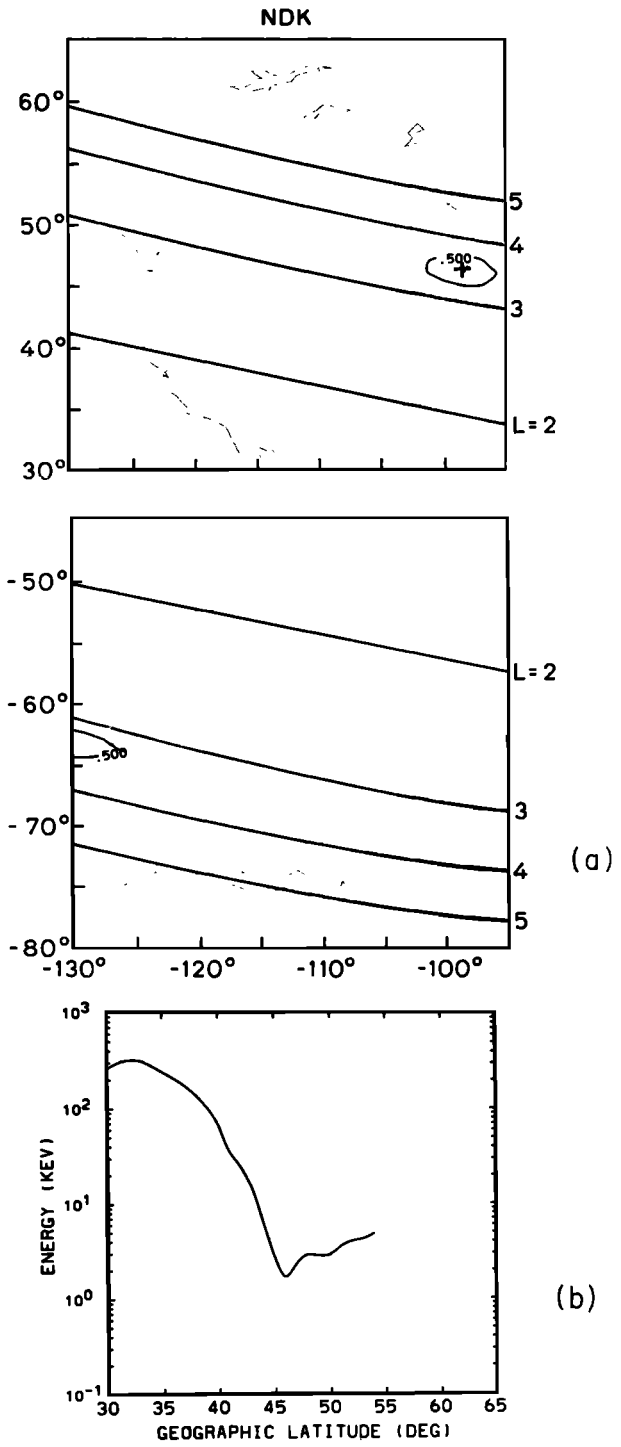

Fig. 13. Precipitation zone around the Omega transmitter in North Dakota, operating at f=13.1 kHz and with P_T=10 kW and its conjugate point. The format is the same as in Figure 8.

contours marked 0.5 in the upper and lower panels of Figure 13 represent roughly the same distance in kilometers.

4.7. Stanford University Experimental Transmitter at Siple, Antarctica

The Stanford University transmitter at Siple, Antarctica has been in operation since 1973 [*Helliwell and Katsufrakis*, 1974]. This is a broadband system, capable of radiating in the 1- to 20-kHz range. In most cases, the transmitter utilizes frequency time formats designed to study various features of magnetospheric wave particle interactions and wave growth and emission triggering in the 2- to 6-kHz range. For the purposes of this paper, we consider operation at 5 kHz with a total radiated power of 3 kW.

Figure 14*a* shows the precipitation zones around the Siple transmitter and its conjugate point. It is interesting to note that the zone is almost symmetric around the location of the transmitter. This is due to the fact that 5 kHz is very

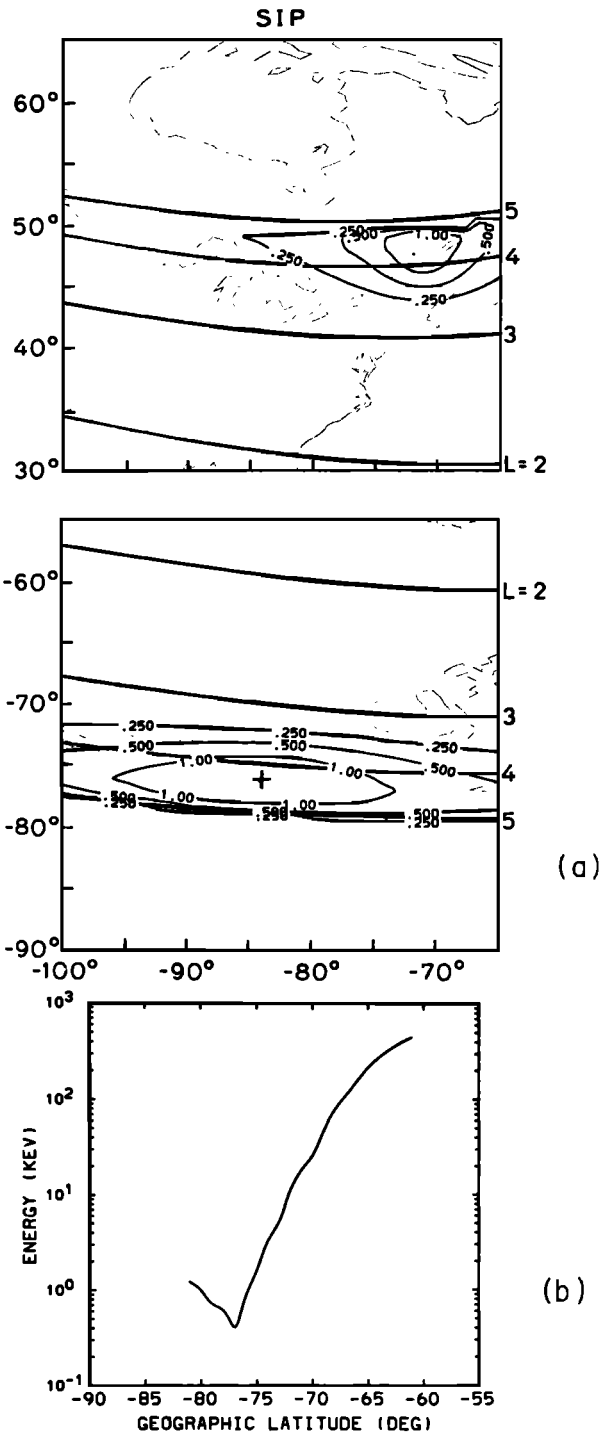

Fig. 14. Precipitation zone around Siple, Antarctica transmitter, operating at f=5 kHz and with P_T=3 kW, and its conjugate point at Roberval, Canada. The format is the same as in Figure 8.

close to the equatorial half gyrofrequency on the Siple field line.

Figure 14b shows the energy of the precipitated particles as a function of latitude for the Siple transmitter. Note that the minimum energy overhead is considerably lower than that for other transmitters. This again is due to the higher L shell of this source as compared to the others.

5. DISCUSSION

In this section we discuss some of the assumptions and models that were utilized in obtaining the results presented above.

5.1. Precipitation Zones: Ducted Versus Nonducted Propagation

We have assumed ducted field-aligned propagation of the transmitter signals in the magnetosphere. Therefore, the precipitation zones of Figures 8–15 represent regions in which the indicated flux levels should be found, to the extent that the region is occupied by whistler mode ducts, or more generally that the medium is suitable for field-aligned propagation of whistler mode wave energy. In this sense these zones represent "potential" precipitation regions in which the indicated fluxes would be expected to be observed if the wave propagation conditions are favorable. Under typical conditions, only a fraction of these regions would be occupied by such ducts. Ground-based observations of lightning-generated whistlers and of VLF transmitter signals indicate that such ducts may exist in $\sim 10\%$ of an overlying region at any given time (D. L. Carpenter, private communication, 1983).

Although strictly speaking we have only considered precipitation due to field-aligned propagating, i.e., ducted waves, a large portion of the wave energy injeced into the magnetosphere from ground based sources propagates in the non-field-aligned, i.e., nonducted, mode [*Smith and Angerami,* 1968; *Bell et al.,* 1981]. The ray paths of these signals can be obtained by ray tracing in a model magnetospheric medium. The wave power density at 1000 km altitude at any point specified by latitute and longitude can still be computed by using (2) and (4). However, the equatorial value of B_w cannot be computed by using (5) since the spreading loss in the nonducted case would in general be different and would depend on the distribution and the spreading of the ray paths. These in turn depend on the background cold plasma density variation that might cause focusing or defocusing of the waves due to the presence of small or large-scale (i.e,plasmapause) irregularities. For the case of a smoothly varying background cold plasma density, the ray paths are also smoothly distributed in an equatorial region of illumination extended over the field lines in the vicinity of the transmitter. In some such cases, the spreading loss between 1000 km altitude and the equator may be roughly the same as the spreading loss in the case of ducted propagation, so that B_{weq} can be estimated by using (5). However, the relatively common occurrence of small-scale irregularities and the variable nature of the plasmapause location and gradients makes such cases rather arbitary and nongeneral.

Even though the equatorial wave intensity B_w can be estimated in some cases, the precipitation induced by the nonducted waves propagating with a finite wave normal angle $\psi > 0°$ cannot be estimated by using our present test particle formulation of the gyroresonant wave-particle interaction. This is because this model is based on the assumption of longitudinal propagation ($\mathbf{k} \| \mathbf{B}_0$, where $\mathbf{B}_0$ is the static magnetic field) with $\psi = 0°$. Cyclotron resonant interactions with obliquely propagating whistler mode waves have until recently not been treated in detail [*Bell,* 1984]. To our knowledge, no working model for estimating the precipitation fluxes induced by such nonducted waves exists at the present time.

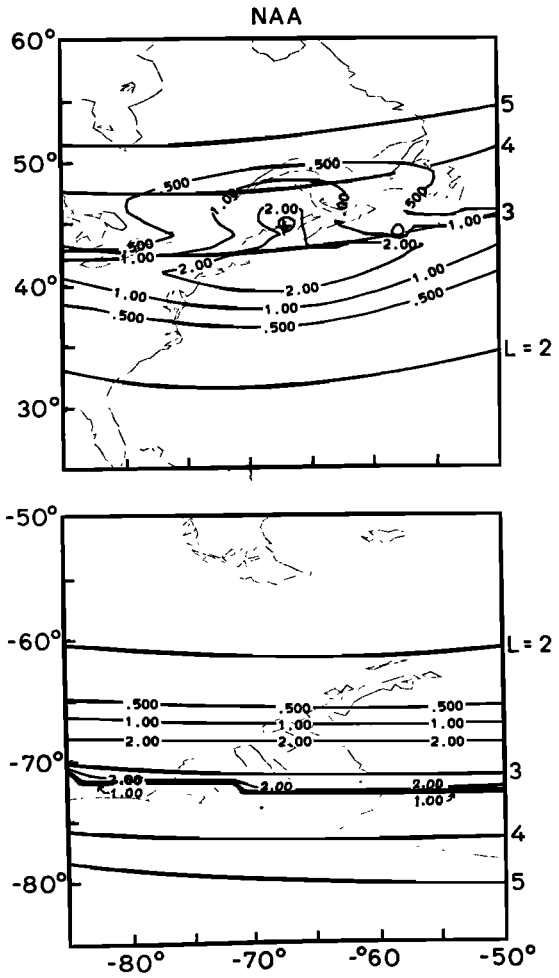

Fig. 15. Precipitation zone around the NAA transmitter and its conjugate point for the case when ~ 10 dB wave amplification at the equatorial plane for $\Lambda < 0.5$ is assumed.

In summary, while the precipitation induced by nonducted waves would be smoothly spread over zones similar to those shown in Figures 8–15, two basic uncertainties exist in the determination of the absolute flux levels. These are (1) estimation of the equatorial wave field intensities B_{weq} based on the ray path distribution which is strongly dependent on the highly variable background cold plasma profile, and (2) estimation of the precipitation fluxes induced by obliquely propagating whistler mode waves. Both these aspects are topics of further study and need to be considered for an overall assessment of energetic particle precipitation induced by manmade waves.

5.2. Wave Growth and Amplification

For the results shown until now, we have considered unamplified VLF waves injected from various transmitters. In the magnetosphere, both natural and manmade signals

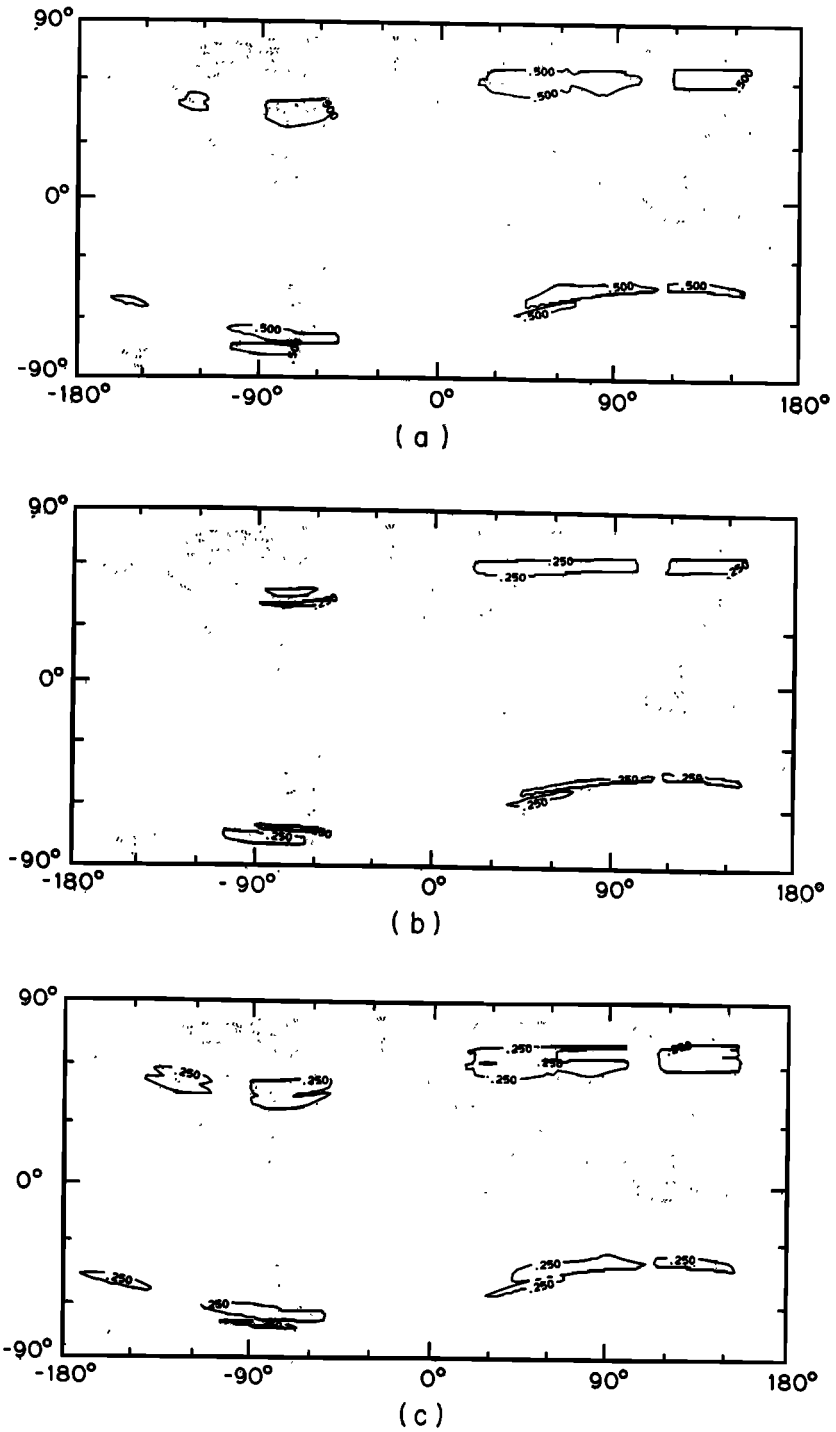

Fig. 16. Global precipitation zones due to the transmitters discussed in this paper. Nighttime conditions over the entire globe (!) is assumed for the purpose of comparison. The top panel shows the zones when particles of all energies are included, the bottom panel shows the zones corresponding to only downcoming particles with energy < 3 keV, and the middle panel shows the same for particles with energy > 3 keV.

are often seen to exhibit growth , amplification, and triggering of emissions. A large base of published data exists on the characteristics of VLF waves that have undergone such amplification and triggering of VLF emissions [*Carpenter and Miller,* 1976; *Helliwell and Katsufrakis,* 1978; *Chang and Helliwell,* 1979, 1980; *Helliwell et al.,* 1980]. Also, theoretical models of the wave-particle interaction mechanism [*Matsumoto et al.,* 1980; *Helliwell and Inan,* 1982] indicate the presence of saturation effects that might limit this growth. It is known that very short wave pulses (<100 ms) do not get amplified and therefore do not trigger emissions [*Helliwell and Katsufrakis,* 1974], whereas the growth of very long pulses may be inhibited because of echo suppression [*Raghuram et al.,* 1977].

Satellite observations have shown that the minimum shift keying (MSK) formats used by some of the communications transmitters (e.g., NAA, NLK, NPM) are not efficient for initiating wave growth and triggering because

the pulse duration at each of the frequencies is limited to 25 ms [*Thomson,* 1981]. Other transmitters, such as those of the Omega network, employ ~1-s long pulses that alternate in frequency and have been seen to be amplified and trigger VLF emissions in the magnetosphere [*Bell et al.,* 1981]. Similarly the Alpha transmitters located in the USSR (see Table 1) , one of which was discussed above (Figure 11) utilize pulsed formats with 400-ms pulses and are often seen to be amplified and trigger emissions [*Inan and Helliwell,* 1982]. The experimental transmitter at Siple, Antarctica, is unique from this point of view since frequency-time formats designed specifically for the purpose of initiating amplification and emission triggering can be employed [*Helliwell and Katsufrakis,* 1974].

Amplification of injected VLF signals by energetic electrons via the gyroresonance interaction mechanism is believed to occur in a region close to the geomagnetic equator [*Helliwell,* 1967]. For most cases of interest, the contributions to the peak precipitated energy flux come from particles that interact with the wave after it traverses the magnetic equator [*Inan et al.,* 1982]. Hence it can be assumed that in cases where wave amplification occurs, the wave intensity and thus the precipitated particle flux will be proportionally higher. As mentioned above, only those signals injected along field lines such that $\Lambda < 0.5$ can stay aligned up to and after the magnetic equator and may thus undergo such amplification.

Figure 15 shows the precipitation zone around the NAA transmitter and the conjugate point in the case where 10 dB amplification is assumed for those signals propagating on field lines where $\Lambda < 0.5$. The result shows an obvious increase in the flux at latitudes for which $\Lambda < 0.5$.

5.3. *Trapped Particle Distribution*

For a given point in the vicinity of the transmitter, the precipitation flux is estimated by interpolating between the values given in Figure 4. These results were obtained [*Inan et al.,* 1982] for a specific model (Figure 3) of the magnetospheric cold plasma and a specific distribution function of the trapped energetic particle population of $f(v,\alpha) = Av^{-n}g(\alpha)$, where we have taken the case of n=6 and $g(\alpha)$=1. Furthermore, the energetic particle distribution $f(v,\alpha)$ and the trapped flux level represented by the differential energy spectrum of Φ_1 was assumed to be the same at all L values. In reality, the available trapped flux is a function of of L value [*Lyons and Williams,* 1975]. The precipitated flux values given in this report are normalized to Φ_1 and thus can be scaled up or down for cases where the numerical value of Φ_1 (in units of el/cm^2 s sr keV) might be known or measured independently. Any L dependent variation of Φ_1 can also be accounted for by scaling the computed flux values by an L dependent factor. The variation of the precipitated flux with L value and Λ will also strongly depend on n, since the resonant particle energy varies with both L and Λ [*Inan et al.,* 1982]. An examination of available data on the trapped radiation in the magnetosphere shows that n may vary from 2 to 8 and Φ_1 may vary over a range of 10^5–10^8 even on the same L value [*Schield and Frank,* 1970; *Lyons and Williams,* 1975]. These variations are due, among other things, to such factors as geomagnetic activity and local time.

Another assumption that was made in obtaining the results of Figure 4 was that of a sharp loss cone for the initial trapped particle distribution. Since the contribution to the precipitated flux comes from the particles that are in the immediate vicinity of the loss cone, the wave-induced flux for a distribution with a tapered loss-cone edge would be less than those given in Figure 4 [*Inan et al.,* 1982].

5.4. *Cold plasma distribution*

Another aspect of the results presented in this paper that needs to be taken into account when applying our results to a specific case is the cold plasma distribution used for our calculations (i.e., Figure 3). The precipitated flux results are dependent on the N_{eq} profile due to two reasons (1) as is apparent from (5) the equatorial wave magnetic field intensity (B_{weq}) for a given input wave power level P_1 depends on the density N_{eq} and (2) as is apparent from (1) the energy of the gyroresonant particles is a function of N_{eq}. The resonant energy in turn determines the efficiency of the interaction and the amount of particle scattering [*Inan et al.,* 1982]. While the first effect mentioned above can be taken into accounted by linearly scaling the flux level in accordance with the different B_{weq}, the dependence of the flux on N_{eq} is a more complicated function of L and Λ and cannot be simply accounted for [*Inan et al.,* 1982].

6. SUMMARY

We have presented estimated spatial distribution of the precipitation zones around existing ground based VLF signal sources and the corresponding conjugate points. These zones are in general much wider in longitude than in latitude and are oriented along lines of constant geomagnetic latitude. The geographic location of the ground-based VLF source and its operating frequency, as well as the radiated power level were seen to be important in determining the size of the precipitation zone.

Figure 16*a* shows a global map of precipitation zones due to ground based VLF signal sources that radiate at power levels > 500 kW with the exception of the Siple transmitter, which is induced due to its unique location and operating frequency. Nightime ionosphere conditions over the entire globe (!) are assumed for the purpose of allowing a comparison of different sources.

Since the energy of the precipitating particles is also computed in our model, the precipitation regions corresponding to various energy ranges can be separately identified. This is especially important since the identification of the precipitation zones is expected to be useful for planning and interpretation of future ground-based experiments, involving instruments and techniques that respond to different particle energies.

As an example, Figure 16b and 16c show the global distribution of precipitation zones that represent the deposition of only >3 keV and <3 keV particles, respectively.

Acknowledgments. This work has greatly benefited from discussions with our colleagues in the Laboratory. We thank A. Leach for her help with the figures. This research was supported by National Science Foundation under contract ATM-80-18248 and by the National Aeronautics and Space Administration under contract NGL-05-020-008. The DE-1 satellite data shown in Figure 2 was acquired and analyzed under contract NAS 5-25688 from the National Aeronautics and Space Administration. The computer calculations were carried out under a Computer Resources grant from the National Center for Atmospheric Research (NCAR) in Boulder, Colorado.

The Editor thanks Bruce Edgar and J. C. Siren for their assistance in evaluating this paper.

REFERENCES

Angerami, J. J., and J. O. Thomas, Studies of planetary atmospheres, 1, The distribution of electrons and ions in the earth's exosphere, *J. Geophys. Res., 69,* 4537, 1964.

Barish, F. D., and R. E. Wiley, World contours of conjugate mirror locations, *J. Geophys. Res., 75,* 6342, 1970.

Bell, T. F., The nonlinear gyroresonance interaction between energetic electrons and coherent VLF waves propagating in an arbitrary angle with respect to the earth's magnetic field, *J. Geophys. Res., 89,* 905, 1984.

Bell, T. F., U. S. Inan, and R. A. Helliwell, Nonducted coherent VLF waves and associated triggered emissions observed on the ISEE-1 satellite, *J. Geophys. Res., 86,* 4649, 1981.

Budden, J. G., *Radio Waves in the Ionosphere,* Cambridge University Press, New York, 1961.

Carpenter, D. L., and J. W. LaBelle, A study of whistlers correlated with bursts of electrons precipitation near $L=2$, *J. Geophys. Res., 87,* 4427, 1982.

Carpenter, D. L., and T. R. Miller, Ducted magnetospheric propagation of signals from the Siple, Antarctica, VLF transmitter. *J. Geophys. Res., 81,* 2692, 1976.

Chang, D. C. D., and R. A. Helliwell, Emission triggering in the magnetosphere by controlled interruption of coherent VLF signals, *J. Geophys. Res., 81,* 7170, 1979.

Chang, D. C. D., and R. A. Helliwell, VLF pulse propagation in the magnetosphere, *IEEE Trans. Antennas Propagat., AP-28,* 170, 1980.

Chang, H. C., and U. S. Inan, Quasi-relativistic electron precipitation due to interactions with coherent VLF waves in the magnetosphere, *J. Geophys. Res., 88,* 318, 1983.

Crary, J. H., The effect of the earth-ionosphere waveguide on whistlers, *Tech. Rep. 9,* Stanford Electron. Labs., Stanford Univ., Stanford, Calif., 1961.

Edgar, B. C., The upper and lower frequency cutoffs of magnetospherically reflected whistlers, *J. Geophys. Res., 81,* 205, 1976.

Helliwell, R. A., *Whistlers and Related Ionospheric Phenomena,* Stanford University Press, Stanford, Calif., 1965.

Helliwell, R. A., A theory of discrete VLF wave emissions from the magnetosphere, *J. Geophys. Res., 72,* 4773, 1967.

Helliwell, R. A., and U. S. Inan, VLF wave growth and discrete emission triggering in the magnetosphere: A feedback model, *J. Geophys. Res., 87,* 3537, 1982.

Helliwell, R. A., and J. P. Katsufrakis, VLF wave injection into the magnetosphere from Siple Station, Antarctica, *J. Geophys. Res., 79,* 2511, 1974.

Helliwell, R. A., D. L. Carpenter, and T. R. Miller, Power threshold for growth of coherent VLF signals in the magnetosphere, *J. Geophys. Res., 85,* 3360, 1980.

Imhof, W. L., E. E. Gaines, and J. B. Reagan, Evidence for the resonance precipitation of energetic electrons from the slot region of the radiation belts, *J. Geophys. Res., 79,* 3141, 1974.

Imhof, W. L., E. E. Gaines, and J. B. Reagan, Observations of multiple, narrow energy peaks in electrons precipitating from the inner radiation belt and their implications for wave-particle interactions, *J. Geophys. Res., 86,* 1591, 1981*a*.

Imhof, W. L., R. R. Anderson, J. B. Reagan, and E. E. Gaines, The significance of VLF transmitters in the precipitation of inner belt electrons, *J. Geophys. Res., 86,* 11225, 1981*b*.

Imhof, W. L., J. B. Reagan, H. D. Voss, E. E. Gaines, D. W. Datlowe, J. Mobilia, R. A. Helliwell, U. S. Inan, and J. P. Katsufrakis, Direct observation of radiation belt electrons precipitated by the controlled injection of VLF signals from a ground-based transmitter, *Geophys. Res. Lett., 10,* 361, 1983.

Inan, U. S., A preliminary study of particle precipitation induced by VLF transmitter signals, *Tech. Rep. E477-1,* Stanford Electron. Labs., Stanford Univ., Stanford, Calif., 1981.

Inan, U. S., and T. F. Bell, The plasmapause as a VLF wave guide, *J. Geophys. Res., 82,* 2819, 1977.

Inan, U. S., and R. A. Helliwell, DE-1 observations of VLF transmitter signals and wave-particle interactions in the magnetosphere, *Geophys. Res. Lett., 9,* 917, 1982.

Inan, U. S., T. F. Bell, D. L. Carpenter, and R. R. Anderson, Explorer 45 and Imp 6 observations in the magnetosphere of injected waves from the Siple Station VLF transmitter, *J. Geophys. Res., 82,* 1177, 1977.

Inan, U. S., T. F. Bell, and R. A. Helliwell, Nonlinear pitch angle scattering of energetic electrons by coherent VLF waves in the magnetosphere, *J. Geophys. Res., 83,* 3235, 1978.

Inan, U. S., T. F. Bell, and H. C. Chang, Particle precipitation induced by short-duration VLF waves in the magnetosphere, *J. Geophys. Res., 87,* 6243, 1982.

ITU, *International Frequency List,* Vol. 1, International Telecommu- nications Union, 1979.

Jensen, D. C., and J. C. Cain, An interim geomagnetic field (abstract), *J. Geophys. Res., 67,* 3568, 1962.

Jordan, E. C., and K. G. Balmain, *Electromagnetic Waves and Radiating Systems,* 2nd ed., Prentice-Hall, Englewood Cliffs, N.J., 1968.

Kintner, P. M., R. Brittain, M. C. Kelly, D. L. Carpenter, and M. J. Rycroft, In situ measurements of transionospheric VLF wave injection, *J. Geophys. Res., 88,* 7065, 1983.

Lyons, L. R., and D. J. Williams, The quiet time structure of energetic(35–560 keV) radiation belt electrons, *J. Geophys. Res., 80,* 943, 1975.

Matsumoto, H., K. Hashimoto, and I. Kimura, Dependence of coherent nonlinear whistler interaction on wave amplitude, *J. Geophys. Res., 85,* 644, 1980.

Park, C. G., D. L. Carpenter, and D. B. Wiggin, Electron density in the plasmasphere: Whistler data on solar cycle, annual, and diurnal variations, *J. Geophys. Res., 83,* 3137, 1978.

Raghuram, R., T. F. Bell, R. A. Helliwell, and J. P. Katsufrakis, Echo-induced suppressions of coherent VLF transmitter signals in the magnetosphere, *J. Geophys. Res., 82,* 2787, 1977.

Scarabucci, R. R., Interpretation of VLF signals observed on the OGO-4 satellite, *Tech. Rep. 3418-2,* Stanford Electron. Labs., Stanford Univ., Stanford, Calif., 1969.

Schield, M. A., and L. A. Frank, Electron observations between the inner edge of the plasma sheet and the plasmasphere, *J. Geophys. Res., 75,* 5401, 1970.

Shawhan, S. D., D. A. Gurnett, D. L. Odem, R. A. Helliwell, and C. G. Park, The plasma wave and quasi-static electric field instrument (PWI) for Dynamics Explorer-A, *Dynamics Explorer,* Dordrecht, D. Reidel, edited by R. A. Hoffman, 1981.

Smith, R. L., and J. J. Angerami, Magnetospheric properties deduced from OGO-1 observations of ducted and nonducted whistlers, *J. Geophys. Res., 73,* 1, 1968.

Smith, R. L., R. A. Helliwell, and I. W. Yarbroff, A theory of trapping of whistlers in field-aligned columns of enhanced ionization, *J. Geophys. Res., 65,* 1839, 1960.

Thomson, N. R., Whistler mode signals: Spectrographic group delays, *J. Geophys. Res., 86,* 4797, 1981.

Vampola, A. L., and G. A. Kuck, Induced precipitation of inner zone electrons, 1, Observations, *J. Geophys. Res., 83,* 2543, 1978.

Wait, J. R., *Electromagnetic Waves in Stratified Media,* Pergamon, New York, 1962.

Walker, A. D. M., The theory of whistler propagation, *Rev. Geophys. Space Phys., 14,* 629, 1976.

Walt, M., W. M. MacDonald, and W. E. Francis, Penetration of auroral electrons into the atmosphere, in *Physics of the Magnetosphere,* edited by R. L. Carovillano, J. F. McClay, and H. R. Radoski, pp. 534–555, D. Reidel, Hingham, Mass., 1968.

H. C. Chang, R. A. Helliwell, and U. S. Inan, Space, Telecommunications and Radioscience Laboratory, Stanford University, Stanford, CA 94305.

(Received June 17, 1983;
revised January 18, 1984;
accepted January 19, 1984.)